Research Article | Vol. 31, No. 18 / 28 Aug 2023 / Optics Express 28792
Optics EXPRESS

Compact oblique-incidence nonlinear widefield microscopy with paired-pixel balanced imaging

TUHIN KHAN,† BEN JOHN,† RICHARDA NIEMANN, ALEXANDER PAARMANN, MARTIN WOLF, AND MARTIN THÄMER*

Department of Physical Chemistry, Fritz Haber Institute of the Max Planck Society, Faradayweg 4-6, 14195 Berlin, Germany
†These authors contributed equally
thaemer@fhi-berlin.mpg.de

Abstract: Nonlinear (vibrational) microscopy has emerged as a successful tool for the investigation of molecular systems as it combines label-free chemical characterization with spatial resolution on the sub-micron scale. In addition to the molecular recognition, the physics of the nonlinear interactions allows in principle to obtain structural information on the molecular level such as molecular orientations. Due to technical limitations such as the relatively complex imaging geometry with the required oblique sample irradiation and insufficient sensitivity of the instrument this detailed molecular information is typically not accessible using widefield imaging. Here, we present, what we believe to be, a new microscope design that addresses both challenges. We introduce a simplified imaging geometry that enables the measurement of distortion-free widefield images with free space oblique sample irradiation achieving high spatial resolution (~1 μm). Furthermore, we present a method based on a paired-pixel balanced detection system for sensitivity improvement. With this technique, we demonstrate a substantial enhancement of the signal-to-noise ratio of up to a factor of 10. While both experimental concepts presented in this work are very general and can, in principle, be applied to various microscopy techniques, we demonstrate their performance for the specific case of heterodyned, sum frequency generation (SFG) microscopy.

1. Introduction

The desire to understand heterogeneous biological, chemical, and physical systems on microscopic length scales has driven the evolution of various microscopy techniques. The oldest and most prominent example is the light microscope which has laid significant foundations for our current knowledge of, for instance, biological processes and functions [1]. Despite this success and the unprecedented spatial resolution that has been realized, conventional optical microscopy has a critical shortcoming for a detailed, comprehensive sample characterization: it lacks chemical specificity. This limitation can be overcome by modern microscopy techniques developed over the last few decades. The most popular among these techniques is undoubtedly fluorescence microscopy, which yields remarkable sensitivity and inherits its chemical specificity from the selective labeling of chemical compounds with appropriate chromophores [2]. The thorough introduction of chromophores into e.g. a biological system is, however, a demanding task, and can, in some instances, be impossible. Furthermore, it can also lead to the creation of entirely different chemical species, which often prevents in vivo studies. Similar considerations apply to many chemical and physical systems.

Alternative, "label-free" methods that combine both chemical specificity and high spatial resolution are typically based on nonlinear vibrational effects such as coherent anti-stokes Raman scattering (CARS) or sum frequency generation (SFG) [3,4]. The vibrational information obtained with these techniques is particularly suited for identifying molecular species and analyzing their structures, and can be employed on virtually any molecular system without the need for labelling

#495903 https://doi.org/10.1364/OE.495903
Journal © 2023 Received 22 May 2023; revised 7 Jul 2023; accepted 10 Jul 2023; published 14 Aug 2023

Optics EXPRESS

[5–12]. Moreover, the vibrational information gets encoded into the generated nonlinear-optical signals, which have frequencies that typically lie in the visible region. Such nonlinear probing of vibrations generally allows for obtaining higher spatial resolution compared to a linear infrared probe with resolutions attaining the sub-micron range, similar to conventional optical microscopy in the visible [13]. Besides these benefits, the physics of the nonlinear light-matter interaction offers additional possibilities for the detailed characterization of molecular species. The nonlinear processes involve the interaction of multiple light beams with the sample and the generated responses are dictated by the corresponding nonlinear susceptibility tensors [14]. These tensors exhibit distinct symmetry properties that can be probed by varying the polarization directions of the pump and probe beams [15,16]. Since the symmetry properties of the susceptibility tensors are directly related to the molecular sample structure such measurements allow for obtaining key information such as molecular orientations or local structural symmetries [14,15,17–19]. In that regard, these nonlinear vibrational techniques create exciting opportunities for microscopy of molecular systems.

Despite the advances made in the past decades it must be noted that nonlinear vibrational microscopy techniques have yet to reach their full potential, mainly due to two technical reasons: (i) the experimental challenge of achieving distortion-free widefield imaging with full polarization-control, and (ii) practical limits of the signal-to-noise level.

Full tunability of induced and detected polarization directions is needed for proper polarization-dependent studies. The z-component of the polarization (orthogonal to the sample surface) is often particularly important as it represents a very distinguished and intrinsically anisotropic direction in most sample systems along which molecular species tend to align [20,21]. To excite the z-component of the polarization the pump beam must irradiate the sample at a non-zero angle with respect to the surface normal. However, such a configuration makes distortion-free widefield imaging very challenging [22]. Another important complication appears when ultrashort broadband laser pulses are used to generate the nonlinear signals which is often the desired approach in nonlinear microscopy [23]. Since all interacting beams (possessing different frequencies) are required to overlap both spatially and temporally at the sample surface a precise and elaborate dispersion control/compensation needs to be implemented whenever the pulses travel through any optical material on the way to the sample (e.g., the objective). This is especially true for phase sensitive measurements as commonly performed in SFG spectroscopy [24]. These technical difficulties have resulted in a situation in which nonlinear vibrational microscopes have been developed and successfully applied, while their full natural strengths being seldom exploited in widefield microscopy applications.

The second key challenge, obtaining high signal-to-noise ratios, is afflicted by the low conversion efficiencies typical for nonlinear processes. This results in the obtained signals being weak and thus challenging to detect. For this reason, the nonlinear signals are usually generated by intense laser pulses. On the other hand, the possibility to increase the signal amplitude by increasing the pump intensities is clearly limited by potential sample damage. This results in a generally poor signal-to-noise ratio or rather long acquisition times, which limits the techniques' broad applicability.

Here we provide solutions for both challenges. In the first part, a new imaging geometry is demonstrated which allows distortion-free widefield imaging with an oblique (tilted) sample irradiation while all beams travel through free space. The presented design is relatively simple, allows for a straightforward alignment, and enables the same ease for more elaborate measurement protocols as in the corresponding spectroscopy applications. Thereafter, in the second part, we address the challenge of the notoriously low signal-to-noise ratios. Here we demonstrate that using a method based on a pixel-to-pixel balanced detection scheme we can significantly improve the S/N (up to a factor of 10), corresponding to a reduction in acquisition time by about two orders of magnitude. For demonstration purposes, these concepts are implemented in a recently

Optics EXPRESS

developed phase sensitive SFG microscope; however, the presented techniques are very general and can, in principle, be employed for any coherent nonlinear microscopy technique.

2. Oblique sample illumination

To excite and probe the z-polarization component in a nonlinear experiment, the pump beams must be in an oblique configuration, with the light collection typically being tilted accordingly. Obtaining spatial resolution with such an approach is relatively trivial when a microscope with a confocal geometry (tight focusing of the pump beams onto the sample combined with single channel detection) is used [25,26]. However, the drawback of this approach is that this requires spatial rastering of the sample, which can lead to a very time-consuming data acquisition depending on the desired field of view (FOV) [27]. This can be avoided, and the data acquisition can be made considerably faster, by using a widefield approach where the desired FOV is illuminated and imaged on a two-dimensional detector chip. Furthermore, eliminating moving components (i.e., sample rastering) highly simplifies the experimental setup. These advantages make widefield imaging attractive for nonlinear microscopy [28,29].

We now discuss several approaches for widefield imaging: In order to acquire the image data in a widefield configuration, the generated light must be collected with an objective. This is, however, non-trivial for oblique illumination. If the objective is tilted according to the incidence beam, the image is distorted such that only a thin line of the sample FOV is in focus (Fig. 1(A)) [30]. The width of the in-focus strip depends on the angle of illumination (between the sample plane and the objective plane) and the objective's numerical aperture (depth of field). These image distortions can be compensated by application of relay imaging (Fig. 1(B)) [22,31,32]. In this design, the light from the sample is projected onto a grating through a relay lens system generating a distortion-free image copy on its surface. The light from this image can then be collected by an objective at normal incidence with respect to the grating surface, producing a distortion-free widefield image on the camera screen. While this procedure is indeed an elegant solution to avoid image distortions it is still an indirect imaging technique and implementing such an approach comes at the cost of a rather complex alignment [32]. Additionally, the spatial resolution in this approach is inherently limited due to the inclined geometry that prevents the use of an objective and a relay lens system with a large numerical aperture (NA).

The only way of directly obtaining a sharp brightfield image without the need to implement such a compensation scheme is to use a geometry where the objective is parallel to the sample surface. This can be combined with oblique excitation beams in two geometries: transmission through the sample from the back side [13,30,33] (Fig. 1(C)) or in reflection mode from the front side (Fig. 1(D)) [34]. In the former case, the sample/substrate needs to be transparent in the frequency range of the pump beams, reducing the microscope's application area. Furthermore, transmitting the possibly ultrashort pump beams through the sample/substrate material requires precise dispersion management and can generate parasitic signal contributions. In reflection mode, a well-resolved widefield image can be acquired by sending the beam through the objective but ensuring the illuminating beam is non-uniform or away from the center, providing finite normal-to-surface optical field components of the pump beams at the interface [34]. Separating pump and signal beam paths is, however, not straightforward for this geometry, especially if multiple frequencies are involved (such as in CARS and SFG). Thus, there is no simple way to collect a widefield distortion-free image in oblique illumination reflection geometry using an off-the-shelf objective.

An alternative (and to our knowledge so far unexplored) approach to overcome this imaging challenge is to choose a geometry where the pump beams irradiate the sample at an oblique angle through the objective (as in Fig. 1(D)), but through free space. To achieve that, however, the objective must contain an off-axis hole. In other words, if one could drill a channel through the lenses without affecting the performance of the objective, it is possible to accomplish the goal.

Optics EXPRESS

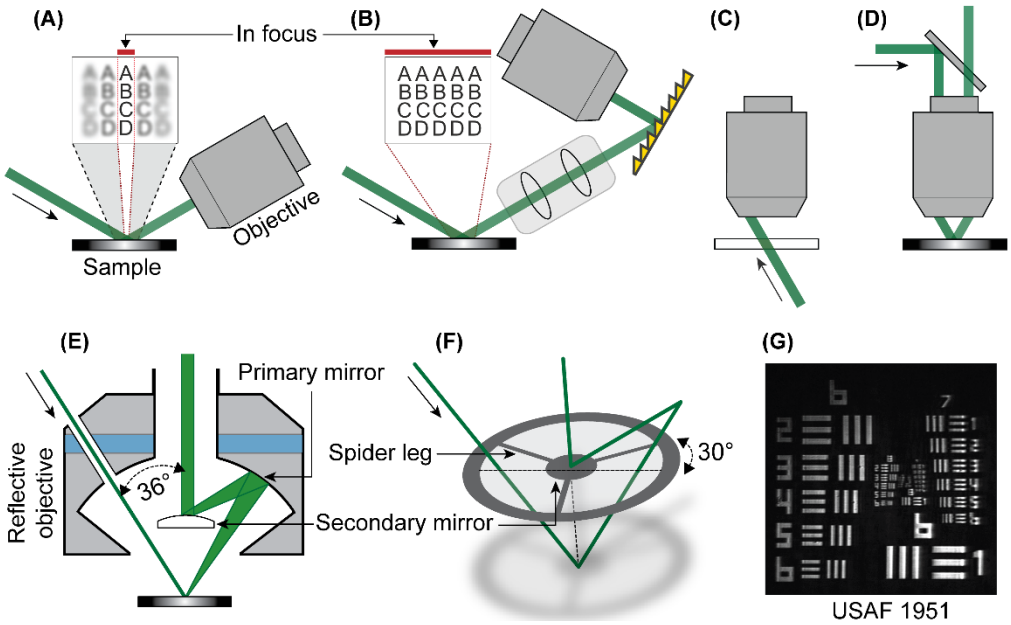

Fig. 1. (A) Conventional widefield imaging at an oblique illumination leads to image distortions; these are corrected using (B) a combination of relay lens and grating. Alternatively, the imaging can be performed (C) in a transmission mode with transparent sample/substrate or (D) in a reflection mode with an asymmetric illumination. (E) We report a new imaging geometry where the illumination is carried through a custom hole in the reflective objective. (F) The hole location ensures proper clearance for both incident and reflected beam through the spider legs. (G) Illumination through this hole resulted in a clear distortion-free image of a standard target sample USAF 1951. The dimension of the image is 260 µm ×260 µm.

Drilling a hole in a lens-based objective would be risky but it can be straightforwardly done using an all-metallic, reflective (Schwarzschild) objective (see Fig. 1(E)). Apart from this rather practical benefit, these reflective objectives have additional advantages as there is no chromatic aberration, and they typically can have larger working distances than the corresponding lens objectives with similar NA. Since the hole size necessary to ensure sufficient clearance for the pump beam delivery to the sample can be relatively small compared to the overall surface area of the primary mirror, there should be no significant degradation of the NA by its presence. It should be noted at this point that widefield imaging with an oblique sample illumination always leads to a certain reduction of the effective NA. However, this is an inherent property of the inclined geometry and cannot be avoided in microscopy applications including the z-polarization component. Therefore, using such a reflective objective to realize the desired oblique illumination imaging geometry seems to be the ideal choice.

For this work, a pure aluminum reflective objective (891-0002, 40x, PIKE Technologies, USA) with a high NA (0.78 NA) is employed, allowing us to achieve high spatial resolution. The objective contains a 5 mm diameter hole drilled in the objective's primary mirror at an angle of 36° with respect to the optical axis (Fig. 1(E)) and with an azimuthal angle of 30° from the closest spider leg (Fig. 1(F)). The incidence angle of 36° ensures proper clearance from the secondary mirror and its spider legs for both the incident and reflected pump beams. Behind the objective, the image is projected onto an EM-CCD camera (ProEM-HS:1024BX3, Teledyne Princeton Instruments, USA) using a 20 cm tube lens. Based on the magnification of the objective (40x) and the pixel size of the CCD chip (13 µm × 13 µm), each pixel corresponds to a theoretical

Optics EXPRESS

sample area of 325 nm × 325 nm. With an expected resolution of ~1 µm, spatial oversampling with the sensor is thus ensured, resulting in the resolution being limited by the effective NA of the optical system.

To test the performance of the described optical configuration, a linear microscopy image of a USAF-1951 (Highres-2, Newport, USA) test sample was recorded by illuminating it with a HeNe laser beam (λ= 632 nm) through the hole in the objective. The resulting image is depicted in Fig. 1 G, showing that a distortion-free widefield image can indeed be recorded using this configuration. The achieved spatial resolution was determined by taking the full width at half maxima (FWHM) of the first derivative of a sharp edge. As shown in Fig. 2, we obtain a resolution of ~1 µm perpendicular to the plane of reflection and ~1.6 µm along the reflection plane. Such anisotropic resolution is expected and originates from the oblique illumination resulting in a reduced effective NA in one direction [22,32,35].

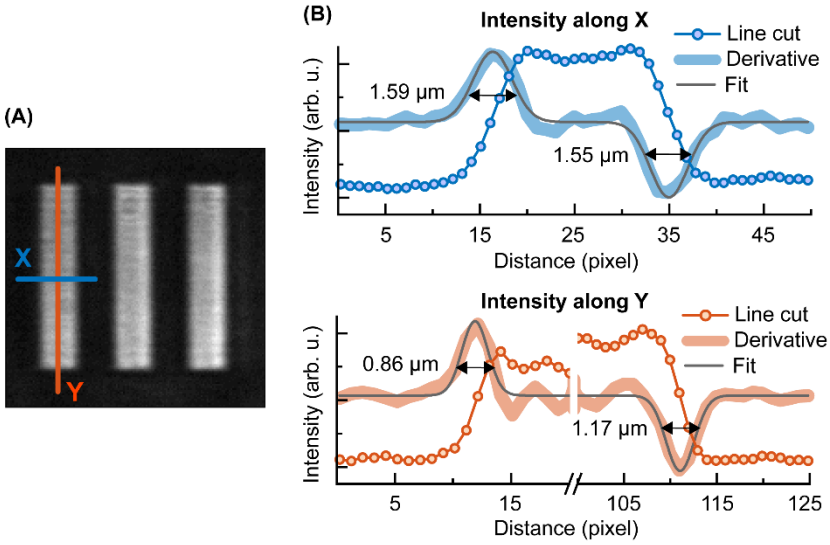

Fig. 2. Analysis of the spatial resolution; (A) widefield linear image of the USAF test target (Group 6, Number 2) using a HeNe laser; (B) slices through the intensity image (above) along the plane of reflection (X) and (below) perpendicular to the plane of reflection (Y). Each plot corresponds to an average of 10 pixels. Resolutions are extracted from the Gaussian fits of the derivative plots.

Overall, we can state that the obtained resolution of roughly 1 µm, achieved across the entire field of view, is a reasonable value for linear optical widefield microscopy given the experimental conditions. However, compared to previous reports of nonlinear microscopy applications employing oblique sample irradiation, the obtained spatial resolution is competitive [5,7,25,36]. On the other hand, it should be noted that the main benefit of the presented imaging geometry is not the improved resolution, but rather the combination of oblique sample irradiation through free space with direct and distortion-free widefield imaging. Our approach bears key advantages in comparison to more commonly used oblique imaging techniques; it allows for straightforward control over the characteristics of the sample excitation, such as polarization directions, relative pulse delays, and illumination spot sizes. At the same time, the alignment is as simple as in a regular light microscope. This simplicity of the imaging geometry opens new possibilities to perform more elaborate measurement protocols and makes it straightforward to transform most of the existing types of nonlinear spectroscopy setups into a nonlinear microscope by simply adding such an objective with the appropriate hole and a camera.

Optics EXPRESS

3. Improving the signal-to-noise ratio

The capability of identifying chemical constituents within a sample and studying their spatial distribution is highly influenced by the achievable signal-to-noise (S/N) ratio in a microscopy experiment. This becomes particularly relevant in nonlinear optical measurements since the generated nonlinear signals are typically weak. The unfortunate square root scaling of the S/N ratio with the number of sampling events limits the possibility of increasing the S/N ratio by temporal averaging. For example, a measurement with a 1/10 S/N ratio in each sampling event with respect to a reference measurement will take about 100 times longer to achieve the same S/N ratio in the final result. This clearly illustrates that relatively small changes in the S/N ratio within the individual sampling events can decide whether an experimental study is feasible. Therefore, any method that increases the S/N ratio is of immense importance in such nonlinear experiments.

Several noise sources contribute to the overall S/N ratio in nonlinear experiments, which can be roughly divided into three categories: i) intensity-independent noise such as background noise, ii) noise scaling with the square root of the signal intensity such as shot noise, and iii) noise scaling linearly with the intensity such as laser intensity fluctuations. Evidently, the impact of the first two types of noise contributions on the S/N ratio can be reduced by increasing the signal intensity, i.e., by increasing the pump beam intensities in the case of a nonlinear experiment. However, as mentioned earlier, this possibility is limited by the damage threshold of the sample and/or the appearance of parasitic higher-order nonlinear effects such as white light generation.

A powerful approach to further enhance the signal intensity without increasing the pump intensity is available if the generated signal is coherent as in SFG or CARS spectroscopy. In these cases, the signal can be heterodyned, i.e., interfered with a relatively strong reference pulse (the so-called local oscillator, LO) yielding a comparatively large interference term that can be recorded. Although the signal enhancement by heterodyning is intrinsically not capable of minimizing the impact of the shot noise, it can raise the signal above the background noise and, therefore, significantly reduce its impact on the S/N ratio [37,38]. The downside of this technique is that the intensity fluctuations of the LO will now become dominant, which highly degrades the improvement in the S/N ratio. This degradation can, however, be overcome by employing a balanced detection scheme where the generated nonlinear signal and the LO are polarized orthogonally and mixed by projection onto a horizontal and a vertical plane after a 45° Jones transformation. The result of this process are two beams: one, which contains constructive- and the other destructive interference with the LO (see Fig. 3(A)) [39–41]. The intensities of these two beams I^+ and I^- respectively, can mathematically be expressed as in Eqs. (1) and (2)

$$I^+ = \frac{1}{2}I_{LO} + \frac{1}{2}I_{NLS} + \sqrt{I_{LO}.I_{NLS}}.\Im(\tau) \tag{1}$$

$$I^- = \frac{1}{2}I_{LO} + \frac{1}{2}I_{NLS} - \sqrt{I_{LO}.I_{NLS}}.\Im(\tau) \tag{2}$$

where I_{LO} and I_{NLS} are the intensities of the local oscillator and the nonlinear signal, respectively. $\Im(\tau)$ describes the intensity-independent interference cross-term between the nonlinear signal and the LO, the quantity of interest. The parameter, τ, indicates its dependency on the relative pulse delays. Comparing Eqs. (1) and (2), we see that by recording these two signals on different detectors and taking the difference of their responses, the interference cross-term can be isolated, and the intensity fluctuations of the LO can efficiently be suppressed (see Fig. 3(B) as an example) [40,42]. This technique of heterodyned balanced detection is well established in various spectroscopic applications, and typical improvements in the S/N ratio of about one order of magnitude can be achieved in nonlinear experiments [39,43,44]. Nevertheless, an adoption of this concept to nonlinear microscopy in a widefield configuration has not yet been realized. As we will show below, this requires a pixel wise approach. One of the main challenges for successfully implementing balanced detection in a nonlinear widefield microscopy setup is that

Optics EXPRESS

the intensity fluctuations measured on an individual pixel on the 2D sensor do not necessarily correlate to the spatially integrated fluctuations of the laser intensity. While the details of the spatial distribution of the intensity are irrelevant in experiments using single-channel detectors, they do matter for widefield imaging. As shown in the simplified schematics in Fig. 4(A), the intensity noise on a single pixel within the 2D sensor can be broken down into three distinct sources: i) overall intensity fluctuations, ii) beam pointing fluctuations, and (iii) mode fluctuations. The overall intensity fluctuations (Fig. 4(Ai)) will be linearly correlated over the entire chip and directly correspond to the spatially integrated intensity fluctuations. By contrast, beam-pointing fluctuations (Fig. 4(Aii)) can result in anti-correlated (left two images in Fig. 4(Aii)) or correlated (right two images in Fig. 4(Aii)) intensity changes with different degrees of nonlinearities in the respective correlation functions depending on the choice of pixels (here exemplified by the green and blue squares). The nonlinearities originate from the non-constant gradient of the 2D intensity profile. Finally, in the case of random mode fluctuations (Fig. 4(Aiii)), there is generally no correlation between the two measured intensity traces. From this theoretical analysis it becomes evident that it can be very hard or even impossible to predict the intensity fluctuations on a single pixel using the information from the spatially integrated intensity or the recorded intensity trace of another pixel.

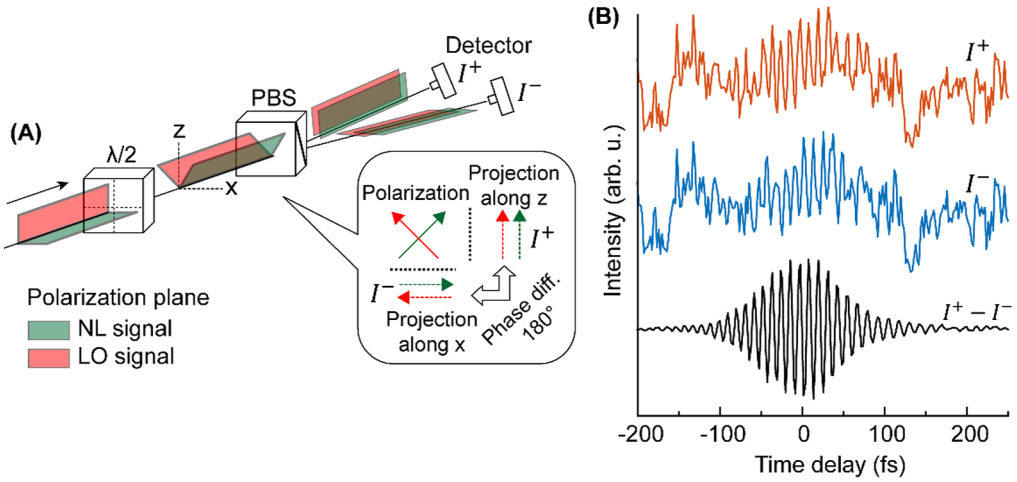

Fig. 3. (A) Principle of balanced detection involving a half waveplate and polarizing beam splitter (PBS) resulting in two 180° phase shifted signals. (B) Heterodyned SFG signal of an Au mirror measured in the time domain using balanced detection with two photodiodes. Subtraction of the two detector responses reveals the resulting S/N (bottom) improvement.

To evaluate to what extent these different sources of intensity noise are relevant in a typical nonlinear microscopy application, we performed a spatial noise correlation analysis using the widefield imaging approach presented in the previous section. For this purpose, a plain Au mirror was used as the sample and the intensity noise in the widefield image was measured and analyzed. As an illumination source, LO pulses (600 nm, ca. 50 fs pulse length at 1kHz repetition rate) were used, being generated from the overlap of a mid-infrared and a visible laser beam in a thin z-cut quartz wafer [39]. The choice of such LO pulses for the illumination of the sample in this measurement is based on the attempt to reproduce the typical experimental setting in heterodyned nonlinear widefield microscopy. Individual noise traces for each pixel were obtained by recording 70 subsequent images with an integration time of 0.5s (corresponding to 500 laser shots).

To visualize the spatial correlation of the intensity noise, a 2D correlation map (Fig. 4(B)) was generated by calculating the Pearson's correlation coefficient of the noise traces for each

Optics EXPRESS

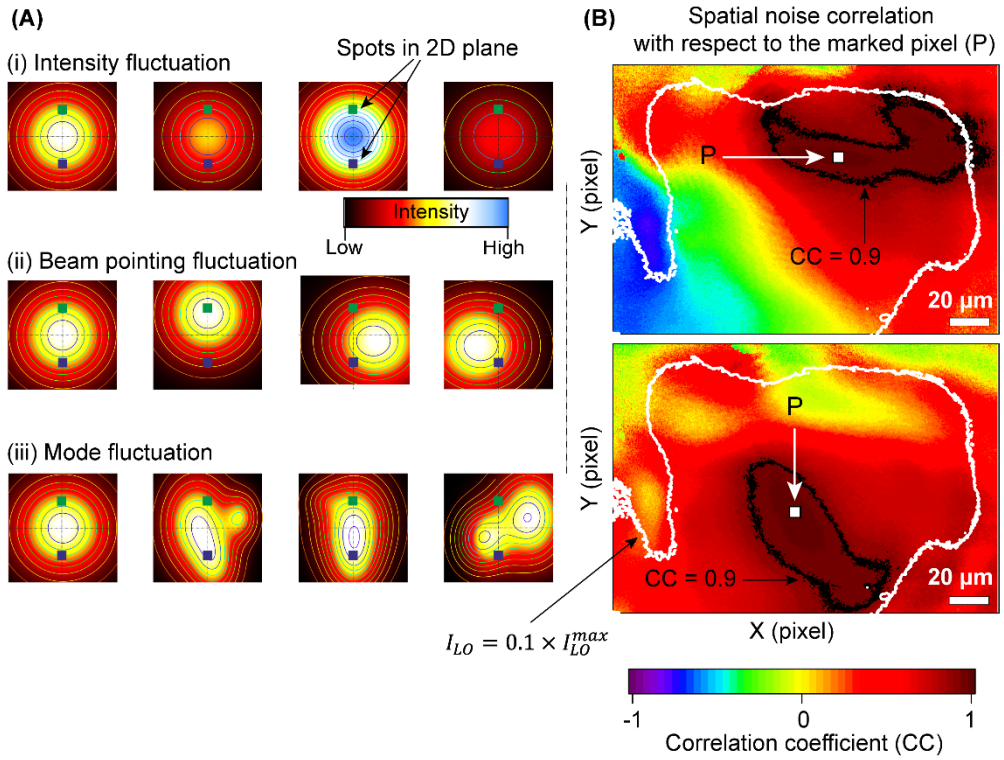

Fig. 4. (A) Schematic depicting possible sources of intensity fluctuation at individual locations (pixels) within the illuminated area. Two pixels, marked by a green and blue square in each image, are highlighted to demonstrate any correlation in the intensity variations due to the different noise sources. (B) Spatial noise correlation maps for an image of an Au mirror recorded with an LO. The correlation coefficients (CC) of the noise traces for each pixel are calculated with respect to the pixel marked by the white square. The white line indicates the region where the LO intensity drops to 10% of the peak value. The black line indicates regions where the correlation value surpasses the value of 0.9 (considered good correlation). The correlation maps are constructed against two exemplary pixels.

pixel with respect to a reference pixel, exemplified for two different reference pixels in the image. By taking the value of 0.9 as an indicator for good correlation, it becomes clear that the noise traces only within the immediate vicinity of the reference pixel are well correlated (appearing as largely asymmetric patches of the order of a few tens of µm). Outside this region, the noise traces quickly become uncorrelated and even turn into regions with slight anticorrelation towards the opposite end of the illumination area. This result indicates that all of the theoretical sources (i-iii) seem to significantly contribute to the detected intensity noise on an isolated pixel, thus presenting a considerable obstacle for implementing a balanced detection system as described above. As this noise analysis was performed with a state-of-the- art nonlinear experimental setup with optimized stability, it is very likely that the determined noise characteristics can be generalized for this type of experiment and that the empirical contributions to the intensity noise are similarly present in most nonlinear microscopes that have been developed.

The noise analysis shown in Fig. 4 suggests that effective implementation of balanced detection in nonlinear widefield microscopy should ideally address the intensity fluctuations on each pixel separately. This can efficiently be achieved by generating two complete images on the camera chip to form pairs of balanced pixels corresponding to the same point on the sample. To realize

Optics EXPRESS

such a dual imaging approach, we introduced a combination of a waveplate and a Wollaston prism (PWK 5.15, B. Halle, Germany) in the beam path behind the objective. That way, we obtain two replicas of the entire image with orthogonal polarization projected onto the camera (Fig. 5(A)). In principle, the intensity fluctuations within these two images should now be fully correlated on the corresponding pixel pairs. In order to test this experimentally, we performed a similar analysis to that depicted in Fig. 4 using a TEM gold grid (grid spacing 42.3 µm) as a sample that we again irradiate with the LO. The waveplate in front of the Wollaston prism is tuned such that equal LO intensities in both images are obtained. We can identify the corresponding pixel pairs with great precision based on the observed grid structure and analyze their noise traces. This analysis reveals that the noise traces of the respective pixels are indeed well correlated, with correlation coefficients over 0.9 across the entire field of view. For illustration, the measured noise traces of two exemplary pixel pairs (a_1, b_1, and a_2, b_2) are depicted in Fig. 5(C). The comparison of the individual traces clearly shows that the corresponding pixel pairs (e.g., a_1 and b_1) show highly correlated intensity modulations. In contrast, non-corresponding pixels (e.g., a_1 and b_2) show vastly differing traces (for better comparability, see the difference traces in Fig. 5(C)). From the result of this experiment, we can conclude that the presented paired-pixel imaging approach can indeed compensate for the intensity fluctuations on an individual pixel.

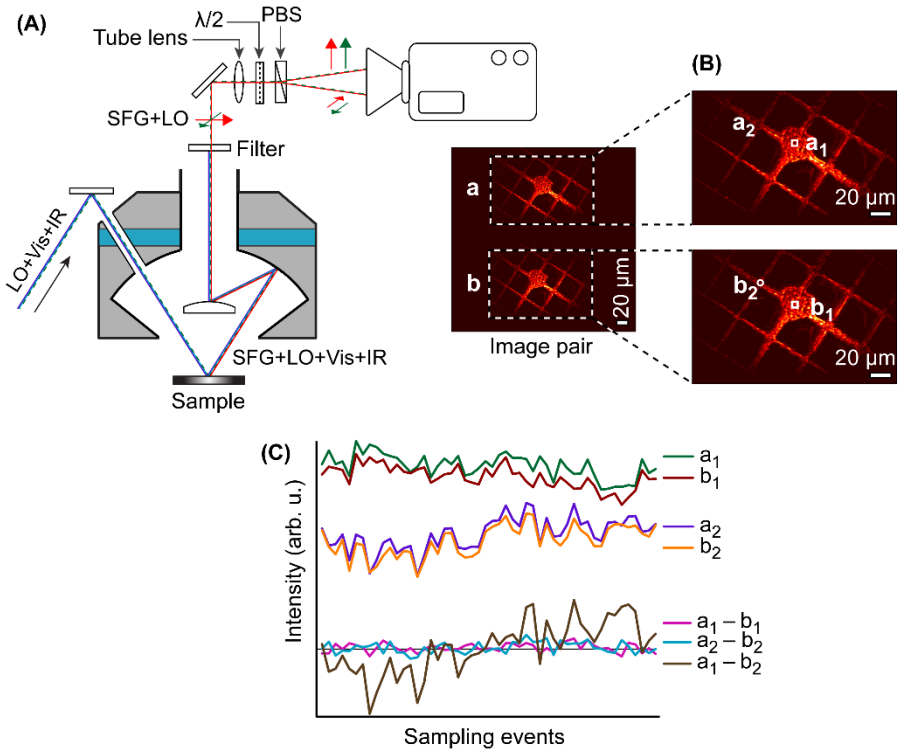

Fig. 5. (A) Schematic of microscope setup including the objective and balanced imaging, (B) extracted image pairs, and (C) time-dependent traces of two pairs of corresponding pixels (a_1 with b_1 and a_2 with b_2).

4. Implementation in a phase-sensitive SFG microscope

In the previous sections the imaging geometry for oblique sample irradiation and the paired-pixel imaging approach were introduced and we have demonstrated their basic functioning in

Optics EXPRESS

experiments using regular linear imaging. In this section we go one step further and demonstrate the performance of these techniques in an exemplary nonlinear microscopy application. For this purpose, both techniques are implemented in a phase-sensitive SFG microscope and nonlinear images from a second TEM gold grid (grid spacing 12.7 µm) are recorded. The choice of this sample type in combination with SFG microscopy bears several advantages: Using p-polarization for both pump beams in this experiment, we generate an exclusively p-polarized SFG signal which arises from the dominating $\chi^{(2)}_{zzz}$ tensor element of the gold layer [45,46]. This is precisely the polarization along the z-axis that is inaccessible with normal incidence illumination used in traditional microscopes. Combined with the fine grid structure of the sample we can therefore directly evaluate the imaging quality of a nonlinear signal for this critical polarization direction. Furthermore, this measurement allows for an experimental analysis of the effective improvement of the S/N ratio in a nonlinear microscopy application using the paired-pixel balanced imaging technique.

The SFG microscope used in this experiment is an extension of our recently developed SFG spectrometer. The details of this instrument can be found elsewhere [39,40], here we only discuss its working principle very briefly: The central part of the spectrometer is a time domain interferometer [39] which includes a full collinear beam geometry and delivers tunable femtosecond pulse sequences of mid-infrared (center frequency 3 µm), visible upconversion (690 nm), and LO pulses. This single output beam is aligned through the hole in the objective and irradiates the sample with a focal spot size of ca. 200 µm (see Fig. 5(A)). The objective collects the nonlinear sample response (SFG) with the reflected LO and the pump beams. After removal of the pump frequencies using a short pass filter, the heterodyned signal is imaged onto the detector chip in dual imaging geometry. The polarization of the LO is tuned to s-polarization, providing orthogonal polarization directions between LO and SFG signal (p-polarized) as required for the balanced detection [39].

The SFG spectra are collected in the time domain by stepwise modifying the relative pulse delays in the interferometer, producing an interferogram in the detected light intensities that is subsequently Fourier transformed. The measurement principle of this technique can thus be seen as the phase-resolved, nonlinear version of a regular Fourier transform infrared (FTIR) spectrometer. Combined with the widefield imaging, we obtain individual interferograms for each pixel within the illuminated area.

A representative 2D raw image from the resulting three-dimensional data set is shown in Fig. 6(A), where the two spatial replicas of the sample response can be observed. The respective time traces for each pixel contain the desired interferogram, offset by the LO intensity. The data contains the discussed intensity noise (see example pixel-pair data shown in Fig. 6(B)). Figure 6(C) shows the corresponding balanced result obtained by subtracting region (b) from region (a) in the raw data. The time traces from this balanced data set now contain the isolated interferogram while the intensity noise is highly suppressed (see the lowest graph in Fig. 6(B)). In order to evaluate the improvement of the S/N ratio within these widefield images, a statistical analysis of all time traces was performed. The resulting 2D maps are shown in Figs. 6(E) and 6(F), respectively. Comparing the two S/N maps (from the region (b) in the raw data and the balanced data set, respectively), it is clear that there is indeed a significant improvement in S/N ratio across the entire field of view by applying the paired-pixel balanced imaging technique. While the obtained values for the S/N ratio in the raw data are in the range from ca. 5-15, the balanced case yields values of ca. 25-50, with the improvement factor varying over the field of view. Overall, typical improvements are about 5x but can reach values up to 10x, as in the example interferogram of the selected pixel shown in Fig. 6(B). The later improvement factor is comparable to the values typically obtained using single-channel balanced detection in the corresponding spectroscopy application [39].

Pixel-wise Fourier transformation of the balanced image data set finally yields the frequency-resolved SFG images of the sample (shown in Fig. 6(D)), along with the resulting SFG spectrum

Optics EXPRESS

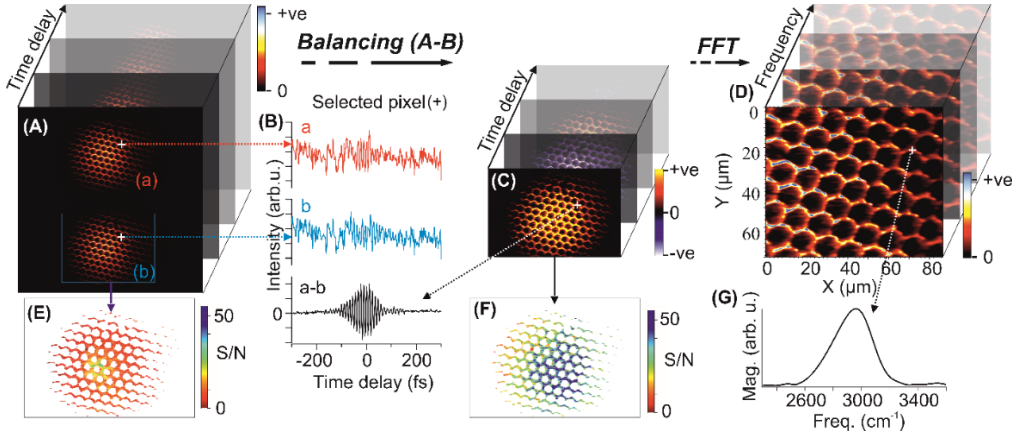

Fig. 6. (A) Time domain SFG images of a gold grid. (B) Interferogram at an individual pixel pair. (C) Balanced images are obtained by subtracting region (b) from region (a) (shown in (A)). (D) Frequency resolved SFG image of the Au grid obtained by Fourier transformation of the 3D data set in (C). The corresponding S/N ratio analysis for the corresponding pixels before balancing (E) and after balancing (F). (G) Resulting SFG magnitude spectrum from the selected pixel.

of the selected single pixel in Fig. 6(G). For clarity, only the magnitude spectrum is depicted, while the phase resolved technique yields both, real and imaginary part of the SFG spectrum for each pixel. Since the nonlinear response of the Au grid is non-resonant, the resulting spectra do not contain any vibrational features beyond the Gaussian-like spectrum of the IR pulses. For the proper evaluation of these results, it is essential to note that the spectrum shown in Fig. 6(G) is a single-pixel spectrum, i.e., it originates from the light generated on a sample spot of only ca. $0.1\mu m^2$ in size. Nevertheless, the obtained spectrum is basically free from noise, and its quality is comparable to spectra that are obtained in the corresponding spatially integrated spectroscopy measurements.

5. Discussion and outlook

The results presented in this work demonstrate that our technique can successfully be employed in nonlinear microscopy applications. The SFG microscopy images of the Au gold grid shown in Fig. 6 were recorded using the described imaging method. The results show that we obtain distortion-free, high-resolution, nonlinear widefield images under oblique sample illumination which gives the desired free access to probing all possible polarization combinations in the nonlinear sample response. The implementation of this imaging geometry therefore yields complete flexibility for polarization-dependent microscopy studies. The other important aspect of our results is the improvement of the S/N ratio by application of the paired-pixel balanced imaging approach. We observe a remarkable increase in S/N of up to a factor of 10. This significant improvement is not only an essential step toward reducing measurement times but can also potentially enable nonlinear microscopy studies, which are currently impossible because of insufficient signal size.

Besides these achievements, one strength of the presented techniques is its straightforward implementation and ease of operation. The presented two methods involve only four critical optical components: the perforated reflective objective, a tube lens, the Wollaston prism, and the camera. Once these four components are aligned (which can easily be done by linear microscopy of a reference sample), performing consecutive, low-noise, nonlinear microscopy measurement

Optics EXPRESS

is as simple as regular linear widefield microscopy. Samples can easily be exchanged, and the only realignment that needs to be done is the proper placement of the sample into the focus of the objective. This also holds for the specific relative positions of the pair pixels within the balanced imaging scheme. These only depend on the alignment of these four fixed components and are relatively independent of exact sample positioning and also even to a certain degree of the beam pointing of the excitation pulses.

Overall, the presented experimental concepts for oblique illumination nonlinear widefield imaging provide new perspectives for coherent nonlinear microscopy studies. Owing to the enormous simplification of the imaging geometry and the significant enhancement of the S/N ratio, these technical solutions represent an essential step toward a new generation of advanced, label-free molecule microscopy experiments. The concepts are general and can, in principle, be applied to any techniques within the diverse family of coherent nonlinear microscopy methods.

Acknowledgments. The authors thank Dr. Sören Waßerroth (FHI) for the helpful discussions, Marcel Krenz and the staff of the central work-shop of the Fritz Haber Institute for fabricating the custom objective. B.J. thanks the International Max Planck Research School for Elementary Processes in Physical Chemistry (IMPRS-EPPC) for support.

Disclosures. The authors declare no conflicts of interest.

Data availability. Data underlying the results presented in this paper are not publicly available at this time but may be obtained from the authors upon reasonable request.

References

1. J. D. Morris and C. K. Payne, "Microscopy and Cell Biology: New Methods and New Questions," Annu. Rev. Phys. Chem. **70**(1), 199–218 (2019).
2. J. W. Lichtman and J. A. Conchello, "Fluorescence microscopy," Nat. Methods **2**(12), 910–919 (2005).
3. W. Min, C. W. Freudiger, S. Lu, and X. S. Xie, "Coherent Nonlinear Optical Imaging: Beyond Fluorescence Microscopy," Annu. Rev. Phys. Chem. **62**(1), 507–530 (2011).
4. J. B. Chao-Yu Chung and E. O. Potma, "Biomolecular Imaging with Coherent Nonlinear Vibrational Microscopy," Annu. Rev. Phys. Chem. **64**(1), 77–99 (2013).
5. S. A. Shah and S. Baldelli, "Chemical Imaging of Surfaces with Sum Frequency Generation Vibrational Spectroscopy," Acc. Chem. Res. **53**(6), 1139–1150 (2020).
6. Y. Han, J. Hsu, N. H. Ge, and E. O. Potma, "Polarization-sensitive sum-frequency generation microscopy of collagen fibers," J. Phys. Chem. B **119**(8), 3356–3365 (2015).
7. H. C. Hieu, N. A. Tuan, H. Li, Y. Miyauchi, and G. Mizutani, "Sum frequency generation microscopy study of cellulose fibers," Appl. Spectrosc. **65**(11), 1254–1259 (2011).
8. K. A. Cimatu and S. Baldelli, "Chemical Microscopy of Surfaces by Sum Frequency Generation Imaging," J. Phys. Chem. C **113**(38), 16575–16588 (2009).
9. T. W. Bocklitz, S. Guo, O. Ryabchykov, N. Vogler, and J. Popp, "Raman Based Molecular Imaging and Analytics: A Magic Bullet for Biomedical Applications!?" Anal. Chem. **88**(1), 133–151 (2016).
10. A. Zumbusch, G. R. Holtom, and X. S. Xie, "Three-Dimensional Vibrational Imaging by Coherent Anti-Stokes Raman Scattering," Phys. Rev. Lett. **82**(20), 4142–4145 (1999).
11. J. X. Cheng and X. S. Xie, "Coherent anti-Stokes Raman scattering microscopy: Instrumentation, theory, and applications," J. Phys. Chem. B **108**(3), 827–840 (2004).
12. C. L. Evans, E. O. Potma, M. Puoris'haag, D. Côté, C. P. Lin, and X. S. Xie, "Chemical imaging of tissue in vivo with video-rate coherent anti-Strokes Raman scattering microscopy," Proc. Natl. Acad. Sci. U. S. A. **102**(46), 16807–16812 (2005).
13. R. Niemann, S. Wasserroth, G. Lu, S. Gewinner, M. De Pas, W. Schöllkopf, J. D. Caldwell, M. Wolf, and A. Paarmann, "Long-wave infrared super-resolution wide-field microscopy using sum-frequency generation," Appl. Phys. Lett. **120**(13), 131102 (2022).
14. P. K. Johansson, L. Schmüser, and D. G. Castner, "Nonlinear Optical Methods for Characterization of Molecular Structure and Surface Chemistry," Top. Catal. **61**(9-11), 1101–1124 (2018).
15. C. Zhang, J. Wang, J. Jasensky, and Z. Chen, "Molecular orientation analysis of alkyl methylene groups from quantitative coherent anti-Stokes Raman scattering spectroscopy," J. Phys. Chem. Lett. **6**(8), 1369–1374 (2015).
16. S. Xu, C. H. Camp, and Y. J. Lee, "Coherent anti-Stokes Raman scattering microscopy for polymers," J. Polym. Sci. **60**(7), 1244–1265 (2022).
17. R. Lu, W. Gan, B. H. Wu, Z. Zhang, Y. Guo, and H. F. Wang, "C-H stretching vibrations of methyl, methylene and methine groups at the vapor/Alcohol (n = 1-8) interfaces," J. Phys. Chem. B **109**(29), 14118–14129 (2005).
18. M. J. Hofmann and P. Koelsch, "Retrieval of complex χ (2) parts for quantitative analysis of sum-frequency generation intensity spectra," J. Chem. Phys. **143**(13), 134112 (2015).
19. M. Cecchini, G. de Vito, V. Piazza, and I. Tonazzini, "RP-CARS: label-free optical readout of the myelin intrinsic healthiness," Opt. Express **22**(11), 13733–13743 (2014).

Optics EXPRESS

20. S. Nihonyanagi, R. Kusaka, K. I. Inoue, A. Adhikari, S. Yamaguchi, and T. Tahara, "Accurate determination of complex χ (2) spectrum of the air/water interface," J. Chem. Phys. **143**(12), 124707 (2015).
21. V. Ostroverkhov, G. A. Waychunas, and Y. R. Shen, "New information on water interfacial structure revealed by phase-sensitive surface spectroscopy," Phys. Rev. Lett. **94**(4), 046102 (2005).
22. Z. Sun, D. Zheng, and S. Baldelli, "Distortion Correction for a Brewster Angle Microscope Using an Optical Grating," Anal. Chem. **89**(4), 2186–2190 (2017).
23. H. Maekawa, S. K. K. Kumar, S. S. Mukherjee, and N.-H. Ge, "Phase-Sensitive Vibrationally Resonant Sum-Frequency Generation Microscopy in Multiplex Configuration at 80 MHz Repetition Rate," J. Phys. Chem. B **125**(33), 9507–9516 (2021).
24. S. Nihonyanagi, J. A. Mondal, S. Yamaguchi, and T. Tahara, "Structure and Dynamics of Interfacial Water Studied by Heterodyne-Detected Vibrational Sum-Frequency Generation," Annu. Rev. Phys. Chem. **64**(1), 579–603 (2013).
25. H. Wang, T. Gao, and W. Xiong, "Self-Phase-Stabilized Heterodyne Vibrational Sum Frequency Generation Microscopy," ACS Photonics **4**(7), 1839–1845 (2017).
26. S. Huang, M. Makarem, S. N. Kiemle, H. Hamedi, M. Sau, D. J. Cosgrove, and S. H. Kim, "Inhomogeneity of Cellulose Microfibril Assembly in Plant Cell Walls Revealed with Sum Frequency Generation Microscopy," J. Phys. Chem. B **122**(19), 5006–5019 (2018).
27. C. Macias-Romero, O. B. Tarun, M. E. P. Didier, V. Zubkovs, P. Marquet, A. Radenovic, S. Roke, P. Jourdain, and P. Magistretti, "High throughput second harmonic imaging for label-free biological applications," Opt. Express **22**(25), 31102–31112 (2014).
28. C. Ceconello, F. Vernuccio, A. D. la Cadena, A. Bresci, F. Manetti, S. Das, R. Vanna, G. Cerullo, and D. Polli, "Wide-field broadband CARS microscopy," EPJ Web Conf. **266**, 08001 (2022).
29. H. Wang and W. Xiong, "Vibrational Sum-Frequency Generation Hyperspectral Microscopy for Molecular Self-Assembled Systems," Annu. Rev. Phys. Chem. **72**(1), 279–306 (2021).
30. M. Flörsheimer, C. Brillert, and H. Fuchs, "Chemical imaging of interfaces by sum frequency microscopy," Langmuir **15**(17), 5437–5439 (1999).
31. J. C. Chastang, "Oblique Viewing Attachment For Microscope," in *Optical System Design, Analysis, and Production*, R. E. Fischer and P. J. Rogers, eds. (SPIE, 1983), 0399(26), pp. 239–245.
32. D. M. P. Hoffmann, K. Kuhnke, and K. Kern, "Chemical imaging of structured SAMs with a novel SFG microscope," Nonlinear Spectrosc. **4812**(1), 82–90 (2002).
33. J. L. Achtyl, M. D. Peterson, E. A. Weiss, I. S. Martinez, P. L. Hayes, L. C. Cass, and F. M. Geiger, "Second harmonic generation imaging with a kHz amplifier," Opt. Mater. Express **1**(1), 57–66 (2011).
34. C. Macias-Romero, I. Nahalka, H. I. Okur, and S. Roke, "Optical imaging of surface chemistry and dynamics in confinement," Science **357**(6353), 784–788 (2017).
35. H.-C. Hsu, L. Li, J. Yao, T. T. W. Wong, J. Shi, R. Chen, Q. Zhou, and L. V. Wang, "Dual-axis illumination for virtually augmenting the detection view of optical-resolution photoacoustic microscopy," J. Biomed. Opt. **23**(07), 1 (2018).
36. I. Toytman, D. Simanovskii, and D. Palanker, "On illumination schemes for wide-field CARS microscopy," Opt. Express **17**(9), 7339–7347 (2009).
37. R. E. Pool, J. Versluis, E. H. G. Backus, and M. Bonn, "Comparative study of direct and phase-specific vibrational sum-frequency generation spectroscopy: Advantages and limitations," J. Phys. Chem. B **115**(51), 15362–15369 (2011).
38. S. Yamaguchi and T. Otosu, "Progress in phase-sensitive sum frequency generation spectroscopy," Phys. Chem. Chem. Phys. **23**(34), 18253–18267 (2021).
39. M. Thämer, R. K. Campen, and M. Wolf, "Detecting weak signals from interfaces by high accuracy phase-resolved SFG spectroscopy," Phys. Chem. Chem. Phys. **20**(40), 25875–25882 (2018).
40. T. Garling, R. K. Campen, M. Wolf, and M. Thämer, "A General Approach To Combine the Advantages of Collinear and Noncollinear Spectrometer Designs in Phase-Resolved Second-Order Nonlinear Spectroscopy," J. Phys. Chem. A **123**(51), 11022–11030 (2019).
41. F. Crisafi, V. Kumar, T. Scopigno, M. Marangoni, G. Cerullo, and D. Polli, "In-line balanced detection stimulated Raman scattering microscopy," Sci. Rep. **7**(1), 10745 (2017).
42. J. E. Laaser, W. Xiong, and M. T. Zanni, "Time-domain SFG spectroscopy using mid-IR pulse shaping: Practical and intrinsic advantages," J. Phys. Chem. B **115**(11), 2536–2546 (2011).
43. S. Ghosh, G. Herink, A. Perri, F. Preda, C. Manzoni, D. Polli, and G. Cerullo, "Broadband Optical Activity Spectroscopy with Interferometric Fourier-Transform Balanced Detection," ACS Photonics **8**(8), 2234–2242 (2021).
44. S. Freitag, M. Baer, L. Buntzoll, G. Ramer, A. Schwaighofer, B. Schmauss, and B. Lendl, "Polarimetric Balanced Detection: Background-Free Mid-IR Evanescent Field Laser Spectroscopy for Low-Noise, Long-term Stable Chemical Sensing," ACS Sens. **6**(1), 35–42 (2021).
45. E. A. Potterton and C. D. Bain, "Infrared-infrared sum-frequency generation from adsorbates on metal surfaces," J. Electroanal. Chem. **409**(1-2), 109–114 (1996).
46. A. G. Lambert, P. B. Davies, and D. J. Neivandt, "Implementing the Theory of Sum Frequency Generation Vibrational Spectroscopy: A Tutorial Review," Appl. Spectrosc. Rev. **40**(2), 103–145 (2005).